OPEN ACCESS

University of BRISTOL

Peer reviewed version

Link to published version (if available):
10.1039/C8TB00709H

Link to publication record in Explore Bristol Research
PDF-document

University of Bristol - Explore Bristol Research
General rights

ARTICLE

Electrically bioactive coating on Ti with bi-layered SnO₂-TiO₂ hetero-structure for improving osteointegration

Rui Zhou,[a,e] Yong Han,*[a] Jianyun Cao,[b] Ming Li,[c] Guorui Jin,[d] Haoteng Luo,[a] Lizhai Zhang [a] and Bo Su *[e]

The potential for the use of electric stimulation to control cell behavior on a surface has been well documented. In terms of orthopedic applications, there is a need to develop bioactive surfaces with a built-in electric field for clinically relevant materials, such as the load-bearing titanium (Ti). In this work, a bi-layered SnO₂-TiO₂ coating is fabricated using microarc oxidation and subsequent hydrothermal treatment to adjust the surface electrical properties for improving bioactivity. The oxidized titanium interlayer on Ti substrate allows the growth of SnO₂ nanorods with different morphologies which leads to a built-in n-n heterojunction of SnO₂ and TiO₂ on Ti surface with varied surface electrical properties. The crystallization of the TiO₂ interlayer facilitates the growth of SnO₂ nanorods, showing excellent hydrophilicity and good apatite-inducing ability due to the formation of heterojunction. The results suggest that the bi-layered SnO₂-TiO₂ coating with electrically stimulated bioactivity could provide a novel way to enhance osteointegration on Ti surface.

Introduction

Electric stimulation offered by externally applied electric fields plays an important role in wound healing and tissue regeneration which can direct cell behavior in a predictable manner. [1,2] An increasing number of studies from recent years have shown that certain electric stimulation can promote *in vitro* osteoblast differentiation and apatite deposition via the change of surface wettability. [3,4] Though some materials have shown the capability to mediate the electric stimulus, such as conductive polymers, piezoelectric and carbon-based materials, [5] the electric stimulus offered by additional equipment is still inconvenient to conduct on an implant for orthopedic applications. Learning how to use such electric stimulation with a built-in electric field and applying them to clinically relevant materials could allow for the development of a new generation of implant surface which can be optimized for bone repair. [5]

Ti and its alloys are some of the most important biomaterials that are commonly used for bone bonding implant application. [6,7] Electric stimulus on Ti surface could be used to control the biological response and improve bone bonding at implant surfaces. [8] In the development of electrically bioactive implant, there is thus a great need for surface designation which can

produce a well-defined built-in electric field to mediate transformation of electron carriers with expected surface charge enrichment, [9] similar to the electric stimulus provided by externally applied electric fields to control the wettability of implant surface. [3]

A promising method for creation of such built-in electric field is the use of heterojunction, which has recently received massive interest for the fabrication of solar cell to promote charge transfer. [9-11] Since the intriguing electron transfer ability of heterojunction with type II band alignment structure can efficiently enhance the separation of electronic carriers, [12] the electron carriers and oxygen vacancies will show the obvious difference in distribution at the heterojunction which can be mediated by the structure of semiconductor layer. [13,14] Fortunately, this phenomenon reveals that a bi-layered heterojunction with a suitable feature on Ti will benefit bioactivity by adjusting surface wettability and receptor response because the oxygen vacancies can react with H₂O to form –OH groups. [15] Meanwhile, the bone tissue is accepted as a piezoelectric material, which can continuously provide the electrical signal during movement, [16] leading to an unbalanced state of the built-in electrical field based on heterojunction. Thus, the long-term availability of the electrically stimulated bioactivity from the heterojunction coating could be ensured, because electron carriers will continuously simulate the surrounding bone tissue based on the response to the unbalanced built-in electrical field.

The hybridization of SnO₂ with TiO₂ as a heterojunction is one of the most appealing solutions to render Ti implant surface with electrical bioactivity, as the band gap of SnO₂ and TiO₂ heterojunction belongs to the type II band alignment structure. [17] Therefore, the electrons will transfer from TiO₂ to SnO₂, benefiting the enrichment of electron carrier on SnO₂, which

a. *State Key Laboratory for Mechanical Behavior of Materials, Xi'an Jiaotong University, Xi'an 710049, P.R. China. E-mail: yonghan@xjtu.edu.cn*

b. *School of Materials, University of Manchester, Manchester M13 9PL, UK.*

c. *Honghui Hospital, Xi'an Jiaotong University College of Medicine, Xi'an 710054, P.R. China.*

d. *Bioinspired Engineering and Biomechanics Center, Xi'an Jiaotong University, Xi'an 710049, P.R. China.*

e. *Bristol Dental School, University of Bristol, Bristol BS1 2LY, UK. E-mail: b.su@bristol.ac.uk*

would be used as the electric stimulation to regulate host tissue response. So far, the bonding between coating and substrate is still a key factor to ensure the success of the application. Fortunately, the coating fabricated by microarc oxidation (MAO) shows excellent bonding with Ti substrate. Meanwhile, both the structure and phase of the TiO_2 based coating can be adjusted by changing processing parameters. [18,19] The effect of TiO_2 crystallinity for the as-designed SnO_2-TiO_2 coating on bioactivity can be investigated. Furthermore, various structures of the nano-sized SnO_2 crystal can be fabricated through hydrothermal treatment, [20] resulting in a bi-layered SnO_2-TiO_2 coating formed on Ti. Because SnO_2 is normally considered as a biocompatible material without bioactivity, even after simulated body fluid (SBF) immersion, [21,22] bi-layered SnO_2-TiO_2 coating would offer a good platform for the investigation of surface electrical properties on osteointegration of Ti implant.

Experimental section

Coating preparation

The pure Ti plates ($10 \times 10 \times 1$ mm^3) and rods ($\Phi 2 \times L6$ mm^3) (Grade II, Baoji Haibao special metal materials Co., China) were ground with 600# and 1000# abrasive papers to wipe off the oxidized layer, and then ultrasonically washed with acetone and distilled water. The Ti plates were used as substrate for surface modification and coating characterization, while the Ti rods were used as the Ti implants for the surface modification and animal surgery. Titanium oxide coating was prepared on Ti substrate via microarc oxidation (MAO) in an electrolyte containing EDTA-2Na (15 g·L^{-1}) and NaOH (7 g·L^{-1}). MAO-Non, MAO-Anatase, and MAO-TiO_2 were labeled as the MAO treated Ti substrates corresponding to the coating phase formed at different applied voltages of 250, 350 and 450 V, respectively. The samples were hanged in the cup and the side towards the bottom of the cup to ensure that the SnO_2 grows without depositions on its surface during the hydrothermal treatment in the solution containing 0.5 g $SnCl_4 \cdot 5H_2O$, 0.7 g NaOH, 30 mL water and 10 mL ethanol, at 200 °C for 24 h. HT-Ti, SnO_2-Non, SnO_2-Anatase, and SnO_2-TiO_2 were used to represent the Ti and MAO coated samples after hydrothermal treatment (Table S1, ESI†).

Characterization

X-ray diffraction (XRD). The phase composition of the plate samples was analyzed by X-ray diffraction (XRD, D/max-gB, Japan).

Scanning electron microscopy (SEM) and energy-dispersive X-ray spectrometer (EDS). Scanning electron microscopy (SEM, Helios Nanolab 600i, FEI Co., USA) was used to observe the surface and facture morphology. Meanwhile, the surface elemental concentrations of the samples were detected by an energy dispersive X-ray spectrometer (EDAX, USA) equipped on the SEM system.

Transmission electron microscopy (TEM). A transmission electron microscopy (TEM, Tecnai G2F30, FEI Co., USA) instrument with an accelerated voltage of 300 kV was used to analyze the microstructure of the SnO_2-TiO_2. Bright and dark field images were used to analyze the morphology of the nanorod. The elemental compositions were analyzed by EDS equipped on the TEM system. The high resolution TEM (HRTEM) pattern was analyzed using the Fast Fourier Transform (FFT) technique to identify the phase of the nanorods. A selected area electron diffraction (SAED) pattern was acquired to analyze the phase of the nanorod.

Contact angle. The contact angles of deionized water on the surfaces were measured using the liquid drop method on a contact angle goniometer (CA, CAM101, KSV Instruments Ltd., Finland).

Zeta-potential. Zeta-potential of the sample surface was determined by a streaming current electro kinetic analyzer (SurPass, Anton Paae GmbH, Graz, Austria). The zeta-potential value was calculated based on Fairbrother-Mastin approach, and 1 mM KCl was used as background electrolyte solution.

Surface roughness. The sample surface was scanned by confocal laser scanning microscope (CLSM, Olympus3000, Japan) over an area of 256×256 µm^2 to calculate the value of surface area roughness (Ra) and peak-to-valley height (Rz).

Fourier transform infrared (FT-IR) spectroscopy. Fourier transform infrared spectroscopy (Magna-IR 560 E.S.P., Nicolet Corp., USA) was used to analyze the deposition formed on the SnO_2-TiO_2 surface after SBF immersion.

X-ray photoelectron spectroscopy (XPS). An X-ray photoelectron spectroscopy (K-Alpha, Thermofisher Scienticfic Co., USA) was used to detect the chemical compositions of the SnO_2-TiO_2 surfaces. In the XPS experiment, an AlKα (1486.6 eV) X-ray source was used for the XPS work under a vacuum of 1.0×10^{-8} mbar. The current of X-ray beam was 6 mA and the resolution for energy was 0.5 eV with a scanning step of 0.1 eV. The regions of 400 µm^2 on the sample surfaces were analyzed. The measured binding energies were calibrated by the C1s (hydrocarbon C–C, C–H) of 284.6 eV. And the chemical states of C, O, Ti and Sn were analyzed.

Electrochemical analysis. The Mott-Schottky plots of the samples were measured on an electrochemical workstation (CHI760E, Shanghai). The voltage was scanned from -0.5 V to 0.5 V versus SCE (saturated calomel reference electrode) at a frequency of 10,000 Hz and 0.5 M Na_2SO_4 was used as the electrolyte. The carrier density of the electrode can be calculated from the intercept and the slope of Mott–Schottky plots using Equation (1).

$$C^{-2} = 2(E - E_{fb} - kT/e)/(N_D \varepsilon \varepsilon_0 e A^2) \qquad \text{Eq. (1)}$$

Where N_D is the carrier density, C is the space charge capacitance, E_{fb} is flat band potential, A is the active surface, ε is the dielectric constant of surface layer, ε_0 is vacuum permittivity, k is the Boltzmann constant, T is the absolute temperature and e is the elementary charge.

Simulated body fluid (SBF) treatment. SBF treatment was used to evaluate the apatite-inducing ability of the samples. [22] The SBF was prepared by dissolving NaCl, $NaHCO_3$, KCl, $K_2HPO_4 \cdot 3H_2O$, $MgCl_2 \cdot 6H_2O$, $CaCl_2$, and Na_2SO_4 in deionized water. Then, it was

buffered at pH 7.40 with tris-hydroxymethylaminomethane ($(CH_2OH)_3CNH_2$) and 1.0 mol L^{-1} HCl at 37 °C. Samples were immersed in it and kept at 37 ℃ for 7 days, and the SBF solution was refreshed very other day.

In vivo experiments

All the animal experiments were complied with the arrive guidelines, which has been approved by the animal care and experiment committee of Xi'an Jiaotong University College of Medicine. To reduce the numbers of animals used in the experiments and minimize the influence of individual differences among rabbits, three holes ($\Phi2 \times L6$ mm³) were drilled through the cortical bone in each tibia of rabbit for placing the Ti, MAO-TiO_2 and SnO_2-TiO_2 implants (Fig. S1, ESI†). Six New Zealand rabbits with the weight of 2.5~3 kg were used in the work.

Surgical procedures. The rabbits were anaesthetized with pentobarbital sodium (40 mg·kg^{-1}) via injecting into the ear vein. The legs were shaved, depilated, and disinfected with iodine. The rabbit was placed on a sterile drape to provide sterile conditions during surgery. After the tibia was exposed by skin incision, holes were drilled in tibia with tooth plant equipment under a cooling condition by saline water for placing implants. The muscular fascia, subcutaneous tissue, and skin were sutured in sequence. Every rabbit was injected with an antibiotic of gentamicin by a dose of 1 mL per day for 3 days. The normal dietary intake by rabbit was performed, and a sutured line was removed after implantation for 10 days.

Sample preparation. The rabbits were chosen randomly to be observed at two periods of 4 and 12 weeks after surgery. The chosen rabbits were sacrificed by the injection of air into the ear vein. Immediately, the tibia was detached from the rabbits for further treatment. Meanwhile, the remained organs were treated safely by the staff of the animal experiment center according to the guidelines.

Radiographic evaluation. The X-ray images of implants were taken by an X-ray 3D imaging system (Y. Cheetah, YXLON International GmbH, Germany) to examine the implantation status.

Histological evaluation. The fluorescence labelling stained sections were directly conducted on an OLYMPUS microscope (CXX41, OLYMPUS, Japan) with fluorescence and white light source, which were analyzed for evidence of bone regeneration at different time of 4, 8, and 12 weeks.

For the fluorescence labelling stain, the tetracycline hydrochloride (10 mg·mL^{-1}, 30 mg·kg^{-1}) and calcein (10 mg·mL^{-1}, 5 mg·kg^{-1}) were subcutaneously injected into the rabbits at different time of 26, 81 and 27, 82 days after surgery, respectively. And the tetracycline hydrochloride (10 mg·mL^{-1}, 30 mg·kg^{-1}) and alizarin red (10 mg·mL^{-1}, 30 mg·kg^{-1}) were subcutaneously injected into the rabbits at different time of 54 and 55 days after surgery, respectively.

The following landmarks were used for histomorphometric measurement of the bone tissue around the implant in the interested zone (IZ) (Fig. S2): the ratios of biological tissue and gap in the fluorescence labeling stained region with a distance

of 500 μm to the cylindrical surface of implants. ImageJ 1.48 software was used for image analyses.

Measurement of push-out force for the implants. The push-out test was carried out using a universal testing machine (Instron-1186, Instron Co., USA) with a penetrator in diameter of 1.8 mm. The fracture surfaces of implants were fixed by 2.5% glutaraldehyde overnight, washed by the PBS and dehydrated in graded ethanol solutions, and then examined by SEM for the failure mode analyses.

Statistical analysis. Three rabbits were used for the histological analyses, while another three rabbits were used for the biomechanical push-out test at 4 weeks after surgery. All the data were expressed as means ± standard deviations (n = 6). The statistical analysis was done by using the IBM SPSS statistical software package. The statistical significance of the difference was measured using a student analysis of variance. The P values <0.05 were considered a statistically significant difference.

Results and discussion

Obviously, the phase formation of MAO coated Ti is dominated by the applied voltage (Fig. 1). Only the typical peaks of α-Ti are observed from the XRD pattern of MAO-Non formed at 250 V, while new peaks of anatase at 25.7° and 38.2° with weak intensity are obtained on the XRD pattern of MAO-Anatase formed at 350 V. As for the XRD pattern of the MAO-TiO_2 which is formed at 450 V, characteristic peaks of both anatase and rutile are obtained. After hydrothermal treatment, new peaks at 26.1°, 33.5°, and 38.3° are observed in every XRD pattern of MAO coated samples, indicating the formation of SnO_2. Interestingly, Ti_8O_{15} but not SnO_2 is formed on the surface of HT-Ti. The reason for this may be attributed to the reaction between NaOH and substrate. Because NaOH is easier to react with Ti than to TiO_2, certain reaction consumes a large amount of NaOH, leading to the change of $SnO_2·xH_2O$ solubility in the bulk solution. Therefore, SnO_2 is difficult to form on Ti surface, because it would be easier for SnO_2 to nucleate and grow in the bulk solution under the supersaturation of $SnO_2·xH_2O$ at lower pH value. [23]

SEM morphologies of Ti and MAO coated Ti samples before and after hydrothermal treatment are shown in Fig. 2. It is clear that the applied voltage significantly changes the surface morphology of MAO treated Ti samples. Some particle-like
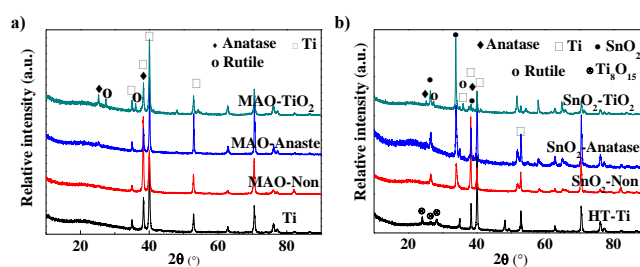

Fig. 1 XRD patterns of Ti and MAO coated Ti samples before and after hydrothermal treatment: a) XRD patterns of samples before hydrothermal treatment, and b) XRD patterns of samples after hydrothermal treatment.

depositions are formed on the surface of MAO-Non, while an oxidized film is formed on the surface of MAO-Anatase according to the EDS results (Fig. S3, ESI†). A typically porous oxidized coating is formed on the surface of MAO-TiO$_2$. After hydrothermal treatment, rod-like films are formed on the MAO coated Ti samples, while the size of the nano-scale rods is greatly affected by the surfaces formed at different applied voltages. With the increase of the applied voltage, the diameter of as-formed nanorod increases, but the inter-distance of the nanorods decreases.

The reasons for the difference in SnO$_2$ generation are mainly attributed to two factors, namely, the surface morphology and the crystal structure matching. Obviously, the rough surface can enhance nuclei due to the heterogeneous nucleation, facilitating the growth of crystal. Regarding the crystal structure matching, TiO$_2$ shows a semi-crystalline match structure with SnO$_2$, which can promote the growth of SnO$_2$ plane (200) along the plane (004) of anatase due to the habit growth relationship. As a result, SnO$_2$ can be generated fast on the surface of MAO coated Ti due to the formation of the oxidized titanium film, attributing to the high crystallinity of TiO$_2$ on MAO-TiO$_2$ and the porous surface structure of the coating which meet the requirements of the nucleation and growth of SnO$_2$. As a result, SnO$_2$ shows fast growth rate on its surface with large nanorod size in diameter. In terms of the MAO-Non, the oxidized titanium film is amorphous phase according to the XRD and EDS results (Fig. 1 and S3, ESI†). Because of the poor crystallinity of oxidized film, it does not facilitate SnO$_2$ growth based on crystal

structure matching. The SnO$_2$ formed on MAO-Non surface shows the relatively low amount and small size (Fig. 2 and S4, ESI†).

In order to further confirm the growth of SnO$_2$ nanorod on MAO coating, the powders on the SnO$_2$-TiO$_2$ surface have been studied by TEM to identify the structure and phase of the coating (Fig. 3). It is clear that the powder collected from the surface consists of two different areas. As for the bright nanorod in the dark field image, it is about 200 nm in diameter and 400 nm in length, and mainly composed of Sn and O. The SAED pattern obtained by FFT is shown in Fig. 3 (b). The spacings of 0.268, 0.185 and 0.337 nm are aspect to the (101), (211) and (110) planes of SnO$_2$, and the angle of 30.1° measured from the SAED pattern is well matched with the theoretical angle of 30.0° between (101) and (211). Regards to the dark substrate area, it is mainly composed of Ti and O. Thus, we can confirm that the oxidized titanium interlayer can facilitate the growth of SnO$_2$ nanorod on its surface.

Fig. 4 shows the contact angle (CA) of deionized water on the MAO coated Ti plates before and after the hydrothermal treatment. The CAs of the MAO coating covered Ti plate show familiar results, which is regularly identified as the hydrophobic surface. After hydrothermal treatment, the surfaces of SnO$_2$-Non and SnO$_2$-Anatase still remain hydrophobic property, while the CA of SnO$_2$-TiO$_2$ decreases to 9.8±1.2° exhibiting an excellent hydrophilic property.

Meanwhile, it is clear from Table 1 that the zeta potential value of the as-formed MAO samples decreases with the increase of applied voltage. This is attributed to the differences in phase and crystallinity of the as-formed MAO coatings (Fig. 1), because crystallized TiO$_2$ shows a more negative surface potential when compared with the amorphous one. [24] Interestingly, the surfaces of samples show more negative surface potential after hydrothermal treatment. As for SnO$_2$-TiO$_2$, its zeta value is -4.99 ± 1.23 mV.
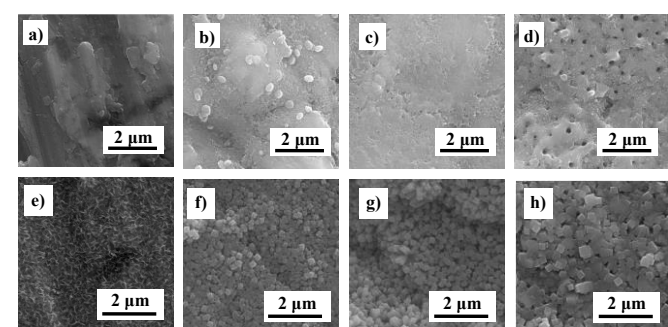

Fig. 2 SEM morphologies of Ti and MAO coated Ti samples before and after hydrothermal treatment: a) Ti, b) MAO-Non, c) MAO-Anatase, d) MAO-TiO$_2$, e) HT-Ti, f) SnO$_2$-Non, g) SnO$_2$-Anatase, and h) SnO$_2$-TiO$_2$.

Table 1 Zeta potential values of the samples without and with SnO$_2$ film.

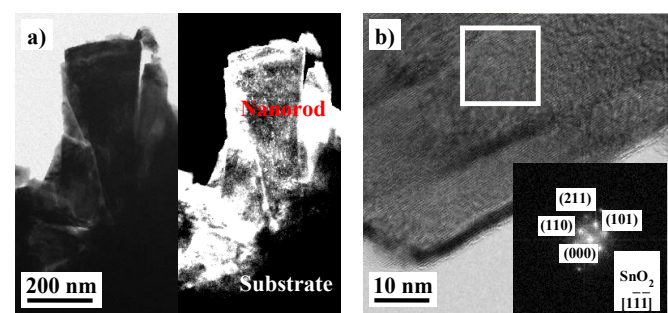| Sample Code	Zeta potential value （mV)	
	without SnO2	with SnO2
MAO-Non	0.09±1.12	-0.50±0.63
MAO-Anatase	-0.50±1.14	-0.93±0.08
MAO-TiO2	-3.56±1.10	-4.99±1.23

Fig. 3 TEM analysis of the nanorod like crystal formed on SnO$_2$-TiO$_2$: a) the bright and dark field TEM morphology, b) HRTEM morphology and SEAD obtained by FFT from the white box area.

Normally, SnO$_2$ is a hydrophilic material and the water CA on smooth SnO$_2$ film is about 20°, and the wettability of SnO$_2$ can also be strongly affected by surface structure. [25] Similar to lotus leaf, the nanorod surface of SnO$_2$ exhibits hydrophobicity, because the air pocket prevents the penetration of the water droplet into the grooves and causes the water droplet suspended on the surface of the films. [26] Herein, though the diameter and inter-distance of the SnO$_2$ nanorod changes, the SnO$_2$ films still show nanorods morphology. According to Cassie and Baxter's model, these surfaces covered with SnO$_2$ nanorods are expected to exhibit hydrophobicity. However, the SnO$_2$-TiO$_2$ surface shows hydrophilicity in this work (Fig. 4). Interestingly, both the hydrophilicity and the negative zeta potential of the
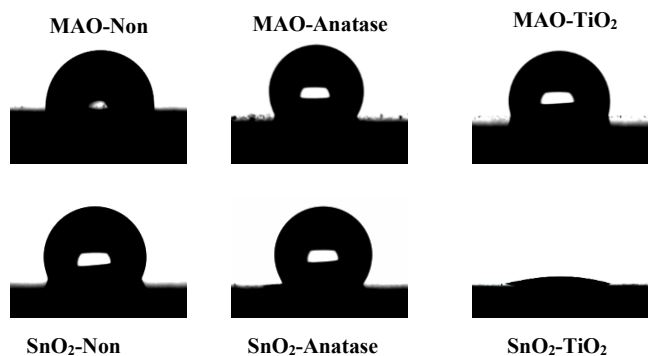
Fig. 4 Contact angle of deionized water on MAO coated Ti samples before and after hydrothermal treatment.

composited coating are closely related to the semi-conductive feature of both SnO_2 and TiO_2, which can normally show a change in wettability from super hydrophobicity to super hydrophilicity under UV-irradiation due to the formation of hole-electron pairs. [27-29] For the SnO_2 or TiO_2 film, some of the holes generated during UV-irradiation can oxidize lattice oxygen to form dissociative oxygen, and oxygen vacancies will form on the surface.[26] Water molecules are more favoured by the defective sites than oxygen molecules in the air because of the strong adsorption between oxygen vacancy and hydroxyl group, leading to the hydrophilicity of the surface. [30] Herein, the SnO_2 and TiO_2 show the type-II band alignment structure which can form an n-n heterojunction to promote charge separation, leading electrons transfer from TiO_2 to SnO_2. [17] Thus, the SnO_2-TiO_2 surface shows more negative zeta potential compared with the MAO coated one because of the enrichment in electrons (Table 1). Meanwhile, the oxygen vacancies generated on the surface are based on the enriched holes, which are formed at the TiO_2 layer near the interface of the bi-layered coating benefiting from the charge separation effect of n-n heterojunction. Attributing to the strong adsorption between vacancy and hydroxyl, the developed SnO_2-TiO_2 surface exhibits excellent hydrophilicity. In addition, the SnO_2 amount on the surface film is also another key point for the charge separation based on the n-n heterojunction. Though electron carriers can be effectively separated on the basis of a small amount of SnO_2 on TiO_2 layer, it cannot provide enough holes and electrons to affect the macroscopic properties of the surface. This point is supported by the results based on short time treated SnO_2-TiO_2. With the varied SnO_2 amount from 11.8 at.% to 14.1 at.%, more electrons would be separated by n-n heterojunction, exhibiting more negative zeta potential vale (between -1.91 mV and -2.78 mV) on the surface than that of SnO_2-Non (-0.50 mV). Meanwhile, similar results have been observed in wettability of SnO_2-TiO_2, it changes from hydrophobicity to hydrophilicity with the prolongation of the soaking time from 4 h to 8 h (Fig.S5, ESI†). Therefore, an enhancement in hydrophilicity of SnO_2-TiO_2 surface is obtained, which is considered as a suitable environment for proteins adsorption and osteoblast attachment. [3,4,31,32]

To confirm this point for the hydrophilic property and negative zeta potential of the SnO_2-TiO_2 surface, the Mott-Schottky plots of the MAO coated Ti samples before and after hydrothermal treatment have been investigated. As shown in Fig. 5(a), the MAO-anatase and MAO-TiO_2 exhibit a positive slope in the MS plots, revealing the formation of n-type semiconductors. Meanwhile, the positive slope increases after the formation of the SnO_2 film, suggesting the n-type semiconductor of SnO_2. Interestingly, the SnO_2-TiO_2 shows a typical n-type semiconductor feature with two different positive slopes around the range of -0.5~0.5 V. Electron carrier densities of SnO_2-TiO_2 in the two different slope areas are calculated to be 7.78×10^{16} cm^{-3} (TiO_2 inner layer) and 4.48×10^{18} cm^{-3} (SnO_2 skin film), respectively. As for the MAO-TiO_2, it is 4.78×10^{17} cm^{-3} (TiO_2 layer), and the electron carrier density of SnO_2-Non is calculated to be 3.23×10^{18} cm^{-3} (SnO_2 film). Based on the results outlined above, we conclude that an n-n heterojunction was constructed on the SnO_2-TiO_2 due to its bi-layered structure (Fig. 5(d)), as the electron carriers obviously transfer from inside TiO_2 layer to the surface SnO_2 film confirmed by the change in their density among the SnO_2-TiO_2, MAO-TiO_2, and SnO_2-Non. Therefore, the negative surface potential and hydrophilicity of SnO_2-TiO_2 would be attributed to the formation of the n-n heterojunction.

Herein, it should be noticed that the performance of semiconductor is closely related to crystal structure, since the band gap would be varied due to the change in phase composition and defective state in crystal lattice. [33,34] In theory, the band gap of anatase is slightly larger than that of rutile, so the charge separation effect of the n-n heterojunction formed by SnO_2 and anatase is expected to be slightly different from that of the heterojunction formed by SnO_2 and TiO_2 (anatase/rutile) based on the band gap. In detail, the conduction band (CB) edges of anatase TiO_2 and SnO_2 are
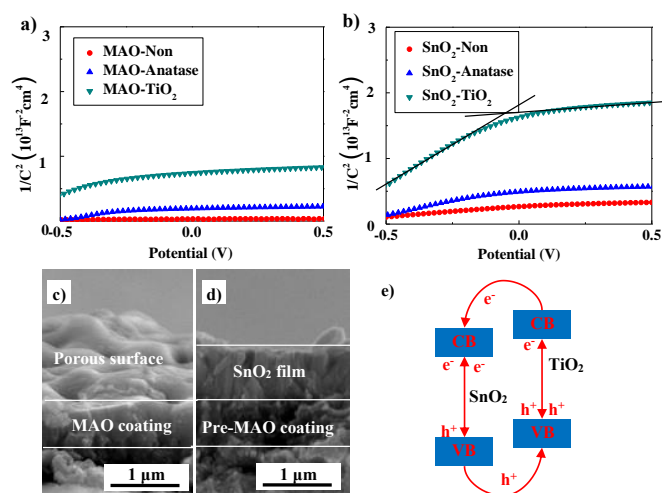

Fig. 5 Mott-Schottky plots and fracture morphologies of the MAO coated Ti before and after hydrothermal treatment: a) Mott-Schottky plots of the MAO coated Ti samples, b) Mott-Schottky plots of the MAO coated Ti samples after hydrothermal treatment, c) and d) fracture morphologies of the MAO-TiO_2 and SnO_2-TiO_2, respectively, e) type-II band alignment structure of SnO_2 and TiO_2.

situated at -0.34 and +0.07 eV versus normal hydrogen electrode (NHE) at pH 7, and the valence band (VB) edge of SnO_2 (+3.67 eV) is much positive than that of anatase TiO_2 (+2.87 eV). [35] This structure belongs to the type II energy band alignment as shown in Fig. 5(e), which can benefit the charge separation. Regarding the rutile TiO_2, a consensus place of the CB for rutile lies 0.2 eV below that of anatase, which should be -0.14 eV. [36-38] The heterojunction formed by SnO_2 and rutile TiO_2 also belongs to the type II energy band alignment, but the charge separation effect is expected to be slightly less than that of the heterojunction formed by SnO_2 and anatase TiO_2 due to the reduction in distance of CBs between TiO_2 and SnO_2. As for the mixed phase TiO_2, both CB and VB should lie between those of anatase and rutile, [37] thus the charge separation effect of the heterojunction formed by SnO_2 and TiO_2 (anatase/rutile) is expected to be slightly less when compared with that of the heterojunction formed by SnO_2 and anatase TiO_2. However, the charge separation effect of SnO_2-TiO_2 is obviously better than that of the SnO_2-anatase. The reason for this should be attributed to the differences in phase and crystallinity of the prepared MAO coatings, which cannot be considered as pure crystal but mixed phase of TiO_2. It is clear that the x-ray diffracion peak intensity of anatase in SnO_2-TiO_2 is 2.23 times stronger than that of SnO_2-anatase with the diffraction peak of Ti substrate as a reference (Fig. 1). This indicates that more anatase has been formed in the previous MAO layer of SnO_2-TiO_2 than that of SnO_2-anatase. Besides, it is also accepted that the MAO coating formed at low applied voltage would be composed of the amorphous phase. [39] Thus, the previous MAO layer in SnO_2-anatase should be considered as a mixed phase of anatase and amorphous TiO_2, but not pure anatase. Furthermore, it has been reported that the pure amorphous TiO_2 is inactive for the photocatalytic reaction. [34] Consistent with this point, the amorphous film of oxidized titanium in MAO-Non cannot show any semiconductor feature according to the Mott-Schottky plot (Fig. 5(a)). Due to the poorer photocatalytic activity of amorphous TiO_2 than that of rutile, the charge separation effect of SnO_2-anatase would be obviously less when compared with that of SnO_2-TiO_2 with relatively high crystallinity. Additionally, Scanlon et al. also reports another possibility of the energy band alignment between anatase and rutile, which indicates that the conduction band edge of anatase lies below 0.2 eV than that of rutile. [11] In this case, even for the pure crystal, the charge separation effect of SnO_2-TiO_2 would obviously larger than that of SnO_2-anatase because of the increase in the distance of CVs and CBs. Based on above discussion, the phase composition and crystallinity of the MAO coating would significantly affect the charge separation effect of the n-n heterojunction in this work.

The XPS spectra detected from the surface of the SnO_2-TiO_2 before and after Ar etching are shown in Fig. 6, from which Ti, Sn, O and C have been detected. Similar Sn 2p and Ti 2p spectra have been obtained before and after Ar etching, the states of Sn^{4+} and Ti^{4+} indicate the formation of the SnO_2 and TiO_2. However, the C 1s and O 1s spectra show obviously different in spectrum after the Ar etching. The divided gaussian peaks of O 1s and C 1s spectra before Ar etching indicate the formation of

hydroxides, C-O, and carbonates on its surface, [40-42] while these peaks are disappeared from the spectrum after Ar etching. This phenome supports the charge separation effect of the n-n heterojunction, because the absorbed H_2O, C and CO_2 are easy to react with oxygen vacancies obtained by charge separation to form the hydroxides, C-O, and carbonates.

Normally, the SnO_2 film is considered as biocompatible materials used in the field of bio-sensor and antibacterial aspects, while no result of bioactivity has been reported even after SBF immersion. [21,22] However, recent investigations indicate that bioactivity not only caused by the chemical composition of the surface, but also the physical properties of the film, especially the electric properties. [1-5] Thus the apatite-inducing ability of the as-formed samples was investigated via 1.5 × SBF immersions for 7 days (Fig. 7) in this work. It is clear that a network film is deposited on the SnO_2-TiO_2 surface (Fig. 7(f)). Combined with the EDS and FT-IR results (Fig. 7(g) and (h)), it is clear that this covered film on SnO_2-TiO_2 is carbonated apatite. However, the other samples retain their surface structure without any deposition indicating the relatively poor bioactivity of the surfaces compared with that of SnO_2-TiO_2. Though some previous works have reported that the TiO_2-based MAO coatings can induce apatite after SBF immersion, but it requires long immersion time for about one month. [43] Herein, the MAO-TiO_2 was immersed in the 1.5 × SBF for only 7 days, thus no apatite was observed on its surface. The bioactivity of SnO_2-TiO_2 is in agreement with a recent report that metal oxides nanoparticles with a negative charge exhibit high calcium-adsorption capacity. [44] Consistent with their result, the SnO_2 film with more negative zeta potential could trigger carbonated apatite nucleation, resulting as good apatite-inducing ability of SnO_2-TiO_2 when compared with the others (Fig. 7).

As the SnO_2-TiO_2 surface shows good apatite-inducing ability and hydrophilicity, the animal experiment is used to evaluate its *in vivo* performance with the control of Ti and MAO-
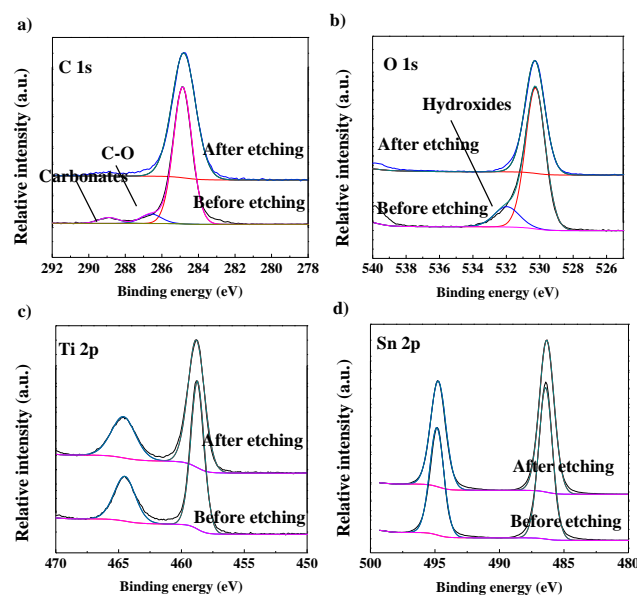

Fig. 6 XPS spectra of the SnO2-TiO2: a) C 1s, b) O 1s, c) Ti 2p, and d) Sn 2p.

TiO$_2$ implants. Fig. 8(a) shows the typical sagittal and coronal radiographs of the Ti, MAO-TiO$_2$ and SnO$_2$-TiO$_2$ implant after healing for 4 weeks. Obviously, the implants do not cause any adverse effects according to the radiographs. Meanwhile, a capsule is formed on tibia surface around the implantation area of SnO$_2$-TiO$_2$ due to the formation of new bone. A thicker bone capsule is observed at the area closer to the implant, showing a radiation-like trend. Besides, the cortical bone shows a tendency to grow along the surface of the SnO$_2$-TiO$_2$ implant in the area between bone and marrow cavity, which is not observed on MAO-TiO$_2$ and Ti implants. These phenomena indicate that the bi-layered SnO$_2$-TiO$_2$ surface can accelerate new bone generation. The reason for this can be explained from two aspects i.e. the formation of apatite and growth of collagen fibers, which are considered as two key attributes for bioactive implant based on the mechanism of osseointegration with surrounding bone tissue. [45] Firstly, the negative charge enriched surface can promote apatite-formation. [44] Consistent with this suggestion, the oxidized titanium surface with densely packed SnO$_2$ nanorods (SnO$_2$-TiO$_2$ surface) which shows more negative surface charge based on heterojunction exhibits better apatite-inducing ability than the ones without heterojunction feature (Fig. 7). Meanwhile, due to the electric properties of the bone tissue, the activity of protein and cell can be activated by the potential difference between the surface and the surrounding tissues. [46] Therefore, SnO$_2$-TiO$_2$ surface provides a suitable environment for bone growth, as it perfectly meets the requirements for the osseointegration of implant.

We believe here the internal electric stimulation played a predominant role rather than the nano-topography of the SnO$_2$-TiO$_2$ surface. As for the nano-topographic patterns created surfaces, integrin lateral clustering as a consequence of ligand density and spacing on materials strongly affects focal adhesion assembly and dynamics of cells. [47-49] A recent work suggests that the TiO$_2$ nanorods with a height of 15 nm and a spacing of 50 nm on Ti surface can enhance osteogenic expression. [50] Ning indicates that the nanorod surface of TiO$_2$ with a height of 23 nm and an optimal spacing of 55 nm on Ti implant could improve bone-bonding strength by 200% compared to that of controlled Ti implant after implantation for 12 weeks. [51] However, the as-formed SnO$_2$ nanorods in this work are densely packed with a height of near 300 nm and a narrow spacing of 20 nm (Fig. 2 and 5(d)), on which cell membranes would be unable to reach surface recesses at the nano intergaps, leading to poor focal adhesion assembly compared with above studies. [47] Furthermore, the surface roughness of the SnO$_2$-TiO$_2$ ($R_a = 0.080 \pm 0.009$ μm and $R_z = 0.348 \pm 0.052$ μm) and MAO-TiO$_2$ ($R_a = 0.079 \pm 0.007$ μm and $R_z = 0.361 \pm 0.042$ μm) shows similar value without any significant difference. Thus, the nanotopography of the developed SnO$_2$ nanorod surface would play but only a limited role in osteogenic differentiation and bone formation, which would be like that of MAO-TiO$_2$ due to the similar surface roughness and morphology (Fig. 2). Instead, both apatite and collagen fibers are prone to form on the electrically bioactive surface of the SnO$_2$-TiO$_2$ implant (Fig. 8(a) and (c)), which may be responsible for significantly enhanced bonding strength between the implant and surrounding bone tissue. As a result, the push-out force of the implant is 77.5 ± 8.2 N (Fig. 8 (b)),
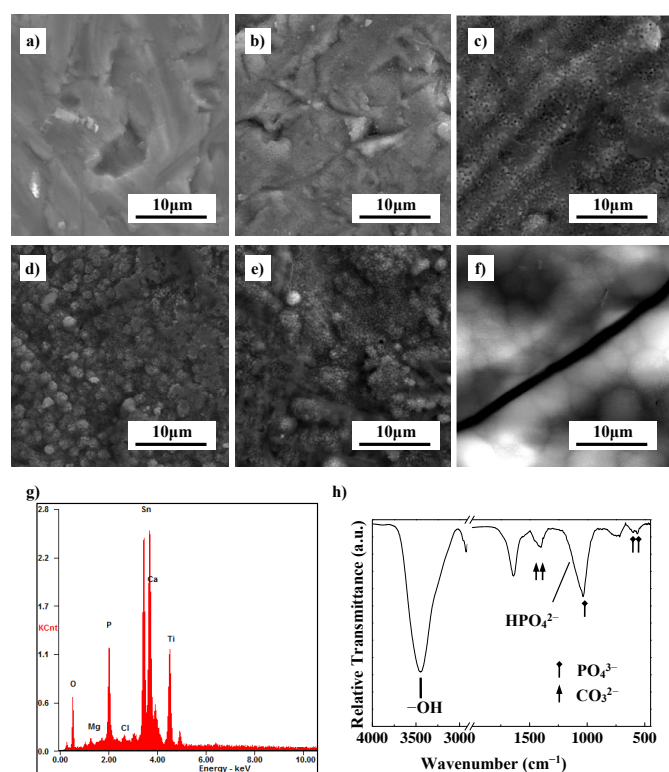

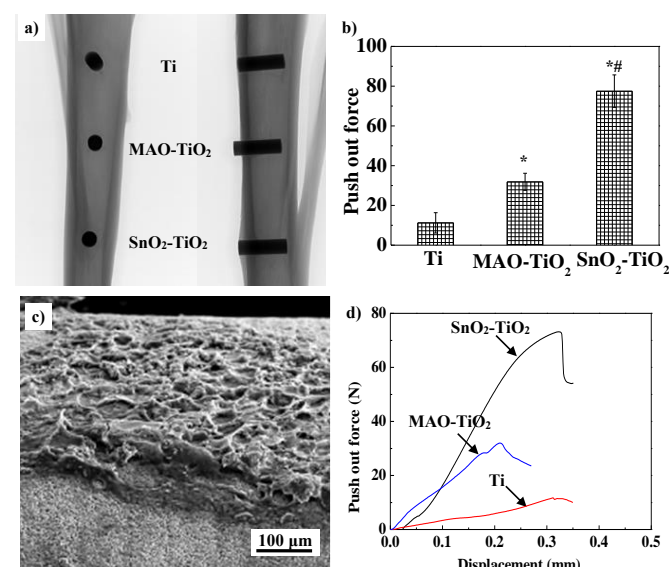Fig. 7 The apatite-inducing ability of the MAO coated Ti before and after hydrothermal treatment: SEM morphology of a) MAO-Non, b) MAO-Anatase, c) MAO-TiO$_2$, d) SnO$_2$-Non, e) SnO$_2$-Anatase, and f) SnO$_2$-TiO$_2$ after 1.5 × SBF immersion for 7 days, g) EDS spectrum of the surface of SnO$_2$-TiO$_2$ after 1.5×SBF immersion for 7 days, and h) FT-IR spectrum of the deposition on the surface of SnO$_2$-TiO$_2$ after 1.5 × SBF immersion for 7 days.

Fig. 8 CT image and push out forces of the Ti, MAO-TiO$_2$ and SnO$_2$-TiO$_2$ implants after healing time of 4 weeks: a) CT image of implants, b) push out forces of implants, c) surface morphology of the pushed out SnO$_2$-TiO$_2$ implant, and d) representative displacement curves of the implants. *$p < 0.05$ compared to the Ti implant, #$p < 0.05$ compared to the MAO-TiO$_2$.

which is nearly 7 times higher than that of pure Ti implant and twice as that of MAO-TiO_2 surface. It should be pointed out that the osteointegration around the implantation area at the early healing stage is still a significant challenge, though many different approaches have been investigated to improve the bioactivity of Ti implant. [52-56] Among these strategies, drug-laden and HA coating on implant surface are two most accepted methods to render Ti with bioactivity due to the excellent *in vivo* performance. [53,54] When compared with the literature values for the push out testing results (Table S2, ESI†), it reveals that the SnO_2-TiO_2 shows similar improvement in bonding strength when compared with the drug-laden or HA coated Ti implants at the early stage of healing, but much better performance compared to the no HA or extracellular matrix (ECM) derived coatings. Thus, the SnO_2-TiO_2 surface with the bi-layered structure on Ti obviously enhances the osseointegration of the implants at the early healing stage of 4 weeks.

In order to ensure the application in long-term load bearing implant, the histological images of the implants after healing of 12 weeks have been also investigated in this work. As observed from the Fig. 9, the green fluorescence lines labeled by brown arrows are pointed to the osteoblast formed at 26 days (4 weeks), the yellow fluorescence lines labeled by blue arrows are pointed to the osteoblast stained at 54 days (8 weeks), while the green fluorescence lines labeled by red arrows are corresponded to the osteoblast formed at 82 days (12 weeks). Therefore, we can distinguish the green fluorescence lines formed at different time easily with the help of the yellow one. After healing of 4 weeks, direct bone-implant contact on the surface of the MAO-TiO_2 and Ti implant is rarely seen, the interface is separated by soft tissue or gaps with wave-like fluorescence lines. Though some gaps have been observed between the SnO_2-TiO_2 surface and the surrounding bone tissue, near half of the interface in cortical region exhibits direct bone-implant contact. This is in consistent with the mechanical test results, SnO_2-TiO_2 shows good push out force with bone tissue at early healing stage (Fig. 8), because most of its surface has been covered by bone tissue. After the surgery for 8 weeks, both the SnO_2-TiO_2 and the MAO-TiO_2 are well covered by bone tissue (synostosis). However, the surrounding bone near MAO-TiO_2 surface shows loose structure due to the formation of cavities in the mineral bone which are labeled by gray arrows in Fig. 9(b). After healing of 12 weeks, the SnO_2-TiO_2 exhibits excellent osteointegration as it is hard to distinguish the newly formed green fluorescence lines at the interface area, while the surface of MAO-TiO_2 in the area close to marrow cavity is still separated by soft tissue or gaps. Regarding to Ti implant, the surface is obviously separated from bone by gaps or soft tissue. This point is strongly supported by the area ratio of gaps in the interested zone (IZ) which is calculated by histological morphometry (Table 2 and Fig. S2, ESI†). Obviously, the bone tissue around SnO_2-TiO_2 shows the densest structure with gap ratio of only 0.44% after healing of 12 weeks, indicating excellent bone regeneration ability. Therefore, the bi-layered SnO_2-TiO_2 coating on Ti substrate shows good bioactivity, which makes it a suitable material for bone tissue replacement and repair.
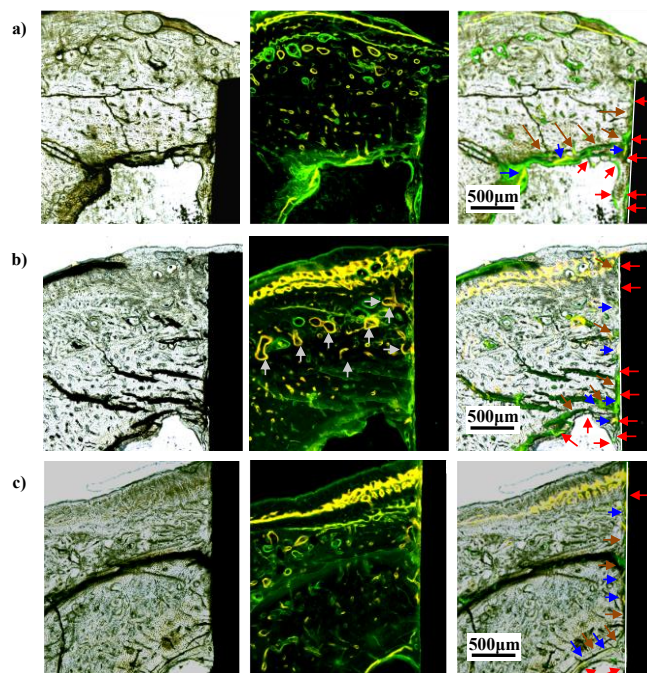

Fig. 9 Histological images, fluorescence labeled images, and the histological images with treble fluorescence labeling at different healing time of 4, 8 and 12 weeks: a) Ti implant, b) MAO-TiO2, c) SnO2-TiO2. (Brown arrow) green fluorescence line labeled at 4 weeks; (blue arrow) yellow fluorescence line labeled at 8 weeks; (red arrow) green fluorescence line labeled at 12 weeks; (white dashed line) the ideal interface between implant and bone tissue; (grary arrow) the cavities formed on bone tissue around MAO-TiO2 after healing time of 4 weeks.

Table 2 The histomorphometry analysis of biological tissue and gap in the interested zoon. (*p < 0.05 compared to the Ti implant, #p < 0.05 compared to the MAO-TiO2.)

Sample code	Gap ratio (%)	Biological ratio (%)
Ti implant	6.27 ± 1.46	93.73 ± 1.46
MAO-TiO2	3.17 ± 0.22 *	96.83 ± 0.22 *
SnO2-TiO2	0.44 ± 0.07 * #	99.56 ± 0.07 * #

Conclusions

A bi-layered SnO_2-TiO_2 coating has been developed on Ti surface via a hybrid technology of microarc oxidation and subsequent hydrothermal treatment. The obtained micro-porous and crystallized TiO_2 coating on Ti substrate is favorable for the growth of the SnO_2 nanorods on the TiO_2 coating, and the crystallinity of TiO_2 is a dominant factor in facilitating the formation of SnO_2-TiO_2 heterojunction. Owing to the formation of n-n heterojunction, the SnO_2-TiO_2 exhibits negative surface potential, superhydrophilicity, and good apatite-inducing ability. Benefiting from its electrically stimulated bioactivity and nanotopographic surface structure, the developed Ti implant with bi-layered SnO_2-TiO_2 coating shows significant improvement in the bonding strength with surrounding bone tissue, which makes it a suitable material for bone tissue replacement and repair.

Notes and references

1   A.H. Rajabi, M. Jaffe and T.L. Arinzeh, *Acta Biomater.,* 2015, **24**, 12–23.
2   A. Campetelli, D. Bonazzi and N. Minc, *Cytoskeleton,* 2012, **69**, 601–612.
3   J. Liao, Y. Zhu, Z. Zhou, J. Chen, G. Tan, C. Ning and C. Mao, *Angew. Chem. Int. Edit.,* 2014, **53**, 13068–13072.
4   R. Hess, A. Jaeschke, H. Neubert, V. Hintze, S. Moeller, M. Schnabelrauch, H.P. Wiesmann, D.A. Hart and D. Scharnweber, *Biomaterials,* 2012, **33**, 8975–8985.
5   C. Ning, L. Zhou and G. Tan, *Mater. Today,* 2015, **19**, 2–3.
6   M. Geetha, A.K. Singh, R. Asokamani and A.K. Gogia, *Prog. Mater. Sci.,* 2009, **54**, 397–425.
7   G. Pan, S. Sun, W. Zhang, R. Zhao, W. Cui, F. He, L. Huang, S.H. Lee, K.J. Shea, Q. Shi and H. Yang, *J. Am. Chem. Soc.,* 2016, **138**, 15078–15086.
8   J. Chen, H.B. Yang, H.B. Tao, L. Zhang, J. Miao, H.Y. Wang, J. Chen, H. Zhang and B. Liu, *Adv. Funct. Mater.,* 2016, **26**, 456–465.
9   C. Ning, P. Yu, Y. Zhu, M. Yao, X. Zhu, X. Wang, Z. Lin, W. Li, S. Wang, G. Tan, Y. Zhang, Y. Wang and C. Mao, *NPG Asia Mater.,* 2016, **8**, e243.
10   V. Pfeifer, P. Erhart, S. Li, K. Rachut, J. Morasch, J. Brötz, P. Reckers, T. Mayer, S. Rühle, A. Zaban, I.M. Seró, J. Bisquert, W. Jaegermann and A. Klein, *J. Phys. Chem. Lett.,* 2013, **4**, 4182–4187.
11   D.O. Scanlon, C.W. Dunnill, J. Buckeridge, S.A. Shevlin, A.J. Logsdail, S.M. Woodley, C.R.A. Catlow, M.J. Powell, R.G. Palgrave, I.P. Parkin, G.W. Watson, T.W. Keal, P. Sherwood, A. Walsh and A.A. Sokol, *Nat. Mater.,* 2013, **12**, 798–801.
12   Y.P. Yuan, L.W. Ruan, J. Barber, S.C.J. Loo and C. Xue, *Energy Environ. Sci.,* 2014, **7**, 3934–3951.
13   J. Shang, W. Yao, Y. Zhu and N. Wu, *Appl. Catal. A-Gen.,* 2004, **257**, 25–32.
14   Y. Li, Y. Yu, Y. Huang, R.A. Goddard, Y. Li and L. Cao, *ACS Catal.,* 2015, **5**, 448–455.
15   C. Mrabet, N. Mahdhi, A. Boukhachem, M. Amlouk and T. Manoubi, *J. Alloy. Compd.,* 2016, **688**, 122–132.
16   A.A. Marino and R.O. Becker, *Nature,* 1970, **228**, 473–474.
17   Z. Liu, D.D. Sun, P. Guo and J.O. Leckie, *Nano Lett.,* 2007, **7**, 1081–1085.
18   J.A. Curran and T.W. Clyne, *Acta Mater.,* 2006, **7**, 1985–1993.
19   R. Zhou, D. Wei, J. Cao, W. Feng, S. Cheng, Q. Du, B. Li, Y. Wang, D. Jia and Y. Zhou, *ACS Appl. Mater. Inter.,* 2015, **7**, 8932–8941.
20   H. Wang and A L. Rogach, *Chem. Mater.,* 2014, **26**, 123–133.
21   M. Patel, J. Singh, M. Singh, V. Agrawal, S.G. Ansari and B. Malhotra, *J. Nanosci. Nanotechno.,* 2013, **13**, 1671–1678.

22   H.K. Varma, K. Sreenivasan, Y. Yokogawa and A. Hosumi, *Biomaterials,* 2003, **24**, 297–303.
23   K. Sato, Y. Yokoyama, J.C. Valmalette, K. Kuruma, H. Abe and T. Takarada, *Cryst. Growth Des.,* 2013, **13**, 1685–1693.
24   J. He, Q.Z. Cai, Q. Luo, D.Q. Zhang, T.T. Tang and Y.F. Jiang, *Korean J. Chem. Eng.,* 2010, **27**, 435–438.
25   M. Miyauchi, A. Nakajima, T. Watanabe and K. Hashimoto, *Chem. Mater.,* 2002, **14**, 2812-2816.
26   W.Q. Zhu, X.J. Feng, L. Feng and L. Jiang, *Chem. Commun.,* 2006, **26,** 2753-2755.
27   Y. Lai, J. Huang, Z. Cui, M. Ge, K. Zhang, Z. Chen and L. Chi, *Small,* 2016, **12**, 2203–2224.
28   K. Liu, M. Cao, A. Fujishima and L. Jiang, *Chem. Rev.,* 2014, **114**, 10044–10094.
29   W. Zhu, X. Feng, L. Feng and L. Jiang, *Chem. Commun.,* 2006, **26**, 2753–2755.
30   R. Sun, A. Nakajima, A. Fujishima, T. Watanabe and K. Hashimoto, *J. Phys. Chem. B,* 2001, **105,** 1984-1990.
31   A. Ranella, M. Barberoglou, S. Bakogianni, C. Fotakis and E. Stratakis, *Acta Biomater.,* 2010, **6**, 2711–2720.
32   L.C. Xu and C.A. Siedlecki, *Biomaterials,* 2007, **28**, 3273–3283.
33   K. Kulbir and C.V. Singh, *Energy Procedia,* 2012, **29**, 291–299.
34   J. Huang, Y. Liu, L. Lu and L. Li, *Res. Chem. Intermediat.,* 2012, **38**, 487–498.
35   M.H. Zhou, J.G. Yu, S.W. Liu, P.C. Zhai and L. Jiang, *J. Hazard. Mater.,* 2008, **154**, 1141-1148.
36   J. Yu, J.C. Yu, W. Ho and Z. Jiang, *New J. Chem.,* 2002, **26**, 607-613.
37   Y. Mi and Y.X. Weng, *Sci. Rep.,* 2015, **5,** 11482.
38   M.E. Arroyo-de Dompablo, A. Morales-Garcia and M. Taravillo, *J. Chem. Phys.,* 2011, **135,** 054503.
39   R. Zhou, D. Wei, H. Ke, J. Cao, B. Li, S. Cheng, W. Feng, Y. Wang, D. Jia and Y. Zhou, *CrystEngComm,* 2015, **17**, 2705–2717.
40   T.K. Sham and M.S. Lazarus, *Chem. Phys. Lett.,* 1979, **68**, 426-432.
41   F.M.F. de Groot, M. Grioni and J.C. Fuggle, *Phys. Rev. B,* 1989, **40**, 5715-5723.
42   A.V. Shchukarev and D.V. Korolkoy, *Cent. Eur. J. Chem.,* 2004, **2,** 347-362.
43   D.Q. Wei and Y. Zhou, *Ceram. Int.,* 2009, **35,** 2343-2350.
44   M. Horie and K. Fujita, *Advances in Molecular Toxicology,* 2011, **5**, 145–178.
45   F.X. Maquart, G. Bellon, B. Chaqour, J. Wegrowski, L.M. Patt, R.E. Trachy, J.C. Monboisse, F. Chastang, P. Birembaut, P. Gillery and J.P. Borel, *J. Clin. Invest.,* 1993, **92**, 2368–2376.
46   C. Halperin, S. Mutchnik, A. Agronin, M. Molotskii, P. Urenski, M. Salai and G. Rosenman, *Nano Lett.,* 2004, **4**, 1253–1256.
47   M. Ventre, F. Causa and P.A. Netti, *J. R. Soc. Interface,* 2012, **9**, 2017–2032.
48   M.J. Dalby, N. Gadegaard, R. Tare, A. Andar, M.O. Riehle, P. Herzyk, C.D.W. Wilkinson and R.O.C. Oreffo, *Nat. Mater.,* 2007, **6**, 997–1003.
49   R.A. Gittens, T. McLachlan, R. Olivares-Navarrete, Y. Cai, S. Berner, R. Tannenbaum, Z. Schwartz, K.H. Sandhage and B.D. Boyan, *Biomaterials,* 2011, **32**, 3395–3403.
50   T. Sjöström, L.E. mcNamara, R.M.D. Meek, M.J. Dalby and B. Su, *Adv. Healthc. Mater.,* 2013, **2**, 1285–1293.
51   C. Ning, S. Wang, Y. Zhu, M. Zhong, X. Lin, Y. Zhang, G. Tan, M. Li, Z. Yin, P. Yu, X. Wang, Y. Li, T. He, W. Chen, Y. Wang and C. Mao, *Sci. Rep.,* 2016, **6**, 19047.
52   Y. Li, S. Zou, D. Wang, G. Feng, C. Bao and J. Hu, *Biomaterials,* 2010, **31**, 3266–3273.
53   M. Nepal, L. Li, T.S. Bae, B. Kim and Y. Soh, *Biomol. Ther.,* 2014, **22**, 563–569.
54   J. Yan, J.F. Sun, P.K. Chu, Y. Han and Y.M. Zhang, *J. Biomed. Mater. Res. A,* 2013, **101**, 2465–2480.

55 K. Takahashi, N. Shiraishi, R. Ishiko-Uzuka, T. Anada, O. Suzuki, H. Masumoto and K. Sasaki, *Int. J. Mol. Sci.,* 2015, **16**, 5779–5788.
56 C. Castllani, R.A. Lindtner, P. Hausbrandt, E. Tschegg, S.E. Stanzl-Tschegg, G. Zanoni, S. Beck and A.M. Weinberg, *Acta Biomater.,* 2011, **7**, 432–440.